Article

Aerosol Detection from the Cloud–Aerosol Transport System on the International Space Station: Algorithm Overview and Implications for Diurnal Sampling

Edward P. Nowottnick [1,*], Kenneth E. Christian [2], John E. Yorks [1], Matthew J. McGill [3], Natalie Midzak [4], Patrick A. Selmer [5], Zhendong Lu [3], Jun Wang [3,6] and Santo V. Salinas [7]

1   NASA Goddard Space Flight Center, Greenbelt, MD 20771, USA
2   Earth System Science Interdisciplinary Center, University of Maryland, College Park, MD 20742, USA
3   Department of Chemical and Biochemical Engineering, The University of Iowa, Iowa City, IA 52242, USA
4   Department of Atmospheric Sciences, University of North Dakota, Grand Forks, ND 58202, USA
5   Science Systems and Applications, Inc., Lanham, MD 20706, USA
6   Interdisciplinary Graduate Program in Informatics, The University of Iowa, Iowa City, IA 52242, USA
7   Centre for Remote Imaging, Sensing and Processing (CRISP), National University of Singapore, Singapore 119076, Singapore
*   Correspondence: edward.p.nowottnick@nasa.gov

Abstract: Concentrations of particulate aerosols and their vertical placement in the atmosphere determine their interaction with the Earth system and their impact on air quality. Space-based lidar, such as the Cloud–Aerosol Transport System (CATS) technology demonstration instrument, is well-suited for determining the vertical structure of these aerosols and their diurnal cycle. Through the implementation of aerosol-typing algorithms, vertical layers of aerosols are assigned a type, such as marine, dust, and smoke, and a corresponding extinction-to-backscatter (lidar) ratio. With updates to the previous aerosol-typing algorithms, we find that CATS, even as a technology demonstration, observed the documented seasonal cycle of aerosols, comparing favorably with the Cloud–Aerosol Lidar with Orthogonal Polarization (CALIOP) space-based lidar and the NASA Modern-Era Retrospective Analysis for Research and Applications, Version 2 (MERRA-2) model reanalysis. By leveraging the unique orbit of the International Space Station, we find that CATS can additionally resolve the diurnal cycle of aerosol altitude as observed by ground-based instruments over the Maritime Continent of Southeast Asia.

Keywords: lidar; aerosol; algorithm; seasonal; diurnal cycle

1. Introduction

Remote sensing of particulate aerosols serves a critical role for determining interactions with the Earth system and adverse impacts on human health. Aerosols can both lead to either positive (warming) or negative (cooling) direct radiative forcing, depending on their composition and placement in the atmosphere, e.g., [1,2]. In addition, aerosols have uncertain but important secondary and higher-order effects on the broader earth system, affecting cloud formation and atmospheric chemistry, e.g., [3,4]. These effects vary depending on aerosol altitude [5–7] and are noted by the Intergovernmental Panel on Climate Change (IPCC) as more uncertain compared to the climate forcings arising from greenhouse gases and other perturbations of the Earth climate system [2]. Beyond their effects on the Earth system, aerosols can have deleterious effects on human health, with small particulates being estimated to cause around 100,000 premature deaths each year in the United States alone [8].

This broad range of effects has led to a variety of different remote sensing instruments being employed in airborne and space-based platforms to determine the abundance and

distribution of aerosols within the atmosphere. Compared to passive instruments, airborne and space-based lidars excel in providing high-resolution vertical profiles of clouds and aerosols. The most recent lidars to operate in orbit designed for cloud and aerosol observations are NASA's Cloud–Aerosol Lidar with Orthogonal Polarization (CALIOP) on the Cloud–Aerosol Lidar and Infrared Pathfinder Satellite Observations (CALIPSO) satellite from 2006 to present [9] and the Cloud–Aerosol Transport System (CATS) aboard the International Space Station (ISS) from 2015 to 2017 [10,11]. CALIOP was originally part of the NASA A-Train constellation of polar-orbiting Earth-observing instruments with a local equatorial crossing time of around 1:30 a.m. and p.m. In contrast, the precessing orbit of the ISS between 51° N–51° S enabled the CATS lidar to observe the vertical distribution of clouds and aerosols at a variety of local times. This variety of times sampled allows the diurnal cycle to be observed with CATS where CALIOP is set with its two equatorial crossing times, e.g., [12,13].

Aerosols exhibit both a seasonal and diurnal cycle because their concentrations and altitudes depend on a variety of factors that vary seasonally and diurnally, including emissions, local meteorology, transport, removal, and chemistry, e.g., [14]. For example, smoke aerosols concentrations are primarily emitted through biomass burning which is highly dependent on local meteorological and source conditions. These conditions vary depending on the season and time of day, e.g., [15], with tropical agricultural burning emissions increasing in the morning ($\sim$1000 local) to an early afternoon peak (1200 to 1400 local) [16,17]. Dust aerosol concentrations likewise vary depending on the regional atmospheric transport and the local conditions at the source regions, e.g., [13,18]. Quantifying the diurnal emission and convective process impacts on the aerosol vertical distributions is essential for determining the aerosol transport pathways and air quality within the planetary boundary layer (PBL) [19–21].

In this study, we describe our most recent aerosol-typing algorithms (V3-00) applied to the 33-month lifetime of the CATS lidar data and compare the seasonal variability in the CATS aerosol type to Modern-Era Retrospective Analysis for Research and Applications, Version 2 (MERRA-2) aerosols and CALIOP observations in Section 2. In Section 3, we leverage the unique orbit of the CATS lidar to quantify the diurnal cycle of smoke aerosols over the Maritime Continent of Southeast Asia and compare this to NASA's ground-based Micro-Pulse Lidar Network (MPLNET) lidar [22]. Our summary and conclusions are discussed in Section 4.

2. CATS Aerosol-Typing Algorithm Description

For the past two decades, backscatter lidars such as the ground-based MPLNET, airborne Cloud Physics Lidar (CPL), and spaceborne CALIOP have demonstrated the ability to determine aerosol types using backscatter and depolarization measurements along with ancillary information. The CATS instrument was built on the heritage of these missions both in instrument design and in its algorithms. As described in Yorks et al. (2016) [11], CATS operated in two science modes. From 10 February 2015 to 21 March 2015, CATS operated in Mode 7.1 which provided 532 and 1064 nm total attenuated backscatter and volume depolarization ratio measurements from two fields of view separated by 7 km on the ground. Beginning 25 March 2015 and through the remainder of operations, CATS operated in Mode 7.2, providing total attenuated backscatter and volume depolarization ratio measurements at 1064 nm from one 0.5° forward field of view. CATS Level 1B (L1B) products such as the total attenuated backscatter, volume depolarization ratio, and associated uncertainties are reported at a 60 m vertical and 350 m horizontal resolution. A detailed description of the CATS cloud–aerosol discrimination (CAD) algorithm and feature confidence scoring is provided in Yorks et al. (2021) [23]. Additionally, as described in Yorks et al. (2021) [23], CATS Level-2 (L2) products such as the feature detection and classification are reported at a 60 m vertical and 5 km horizontal resolution. For daytime CATS granules, a coarser horizontal (60 km) averaging of the L1B products is regularly used to increase the signal-to-noise ratio (SNR) for improved feature detection in scenes

with high solar background contributions; however, the products are still reported at a 5 km horizontal resolution.

The CATS aerosol-typing algorithm leverages the V3 CALIOP aerosol-typing algorithm [24]. However, because CATS operated in Mode 7.2 for most of its lifetime, the primary observable inputs to the CATS algorithm are at 1064 nm, as opposed to 532 nm used by CALIOP. The observed inputs to the CATS operational aerosol-typing algorithm include feature-integrated total attenuated backscatter (sr^{-1}) at 1064 nm (γ'_{1064}), feature-integrated volume depolarization ratio (defined as the ratio between the perpendicular total backscatter to the parallel total backscatter) at 1064 nm (δ'_{1064}), and the feature-integrated spectral volume depolarization ratio ($\delta'_{1064}/\delta'_{532}$), though the latter input is available only in Mode 7.1. In addition to the observed quantities, the CATS aerosol-typing algorithm uses ancillary information, such as the surface type from the International Geosphere–Biosphere Programme (IGBP) [25], feature thickness and elevation, and aerosol typing provided by MERRA-2, as described later in this section.

The Mode 7.1 operational aerosol-typing algorithm classifies eight aerosol types: desert dust, dust mixture, smoke, polluted continental, clean/background, marine, marine mixture, and upper troposphere–lower stratosphere (UTLS) aerosol (Figure 1). Based on the CPL observations of Saharan dust from the NASA Tropical Composition, Cloud, and Climate Coupling (TC^4) [26] and Hurricane and Severe Storm Sentinel (HS3) [27] field campaigns, desert dust features are identified when δ'_{1064} is greater than 0.25. A dust mixture, which is meant to characterize desert dust mixed with other aerosol types such as smoke and marine aerosol types, is classified when δ'_{1064} is greater than 0.15 and less than or equal to 0.25. For spherical aerosols (low depolarization ratios) and owing to similar minimal detectable backscatter (MDB) between CATS at 1064 nm and CALIOP at 532 nm [11], a clean/background type is assigned to layers with γ'_{1064} less than 0.0005 sr^{-1}, as in the CALIOP V3 aerosol-typing algorithm. Utilizing the IGBP land-surface classification, marine and marine mixture aerosol layers are classified for low depolarizing layers over water that are not elevated. The CATS operational aerosol-typing algorithm modified the CALIOP V3 definition of an elevated aerosol layer to classify elevated aerosol layers as those with at least a 1 km separation between the layer base and the surface and at least 2 km in thickness. This modification is based on Nowottnick et al. (2015) [28], who found that the CALIOP V3.01 definition of an elevated aerosol layer classified transported smoke layers over the ocean as marine over the central Atlantic Ocean. Backscatter lidars, such as CATS, measure the volume depolarization ratio, which includes both molecular and particulate depolarization contributions. To help discriminate marine from marine mixture layers, the feature-integrated spectral volume depolarization ratio ($\delta'_{1064}/\delta'_{532}$) is used because polluted marine layers exhibit a greater spectral particulate depolarization ratio than clean marine layers [29]. In CATS Mode 7.1, the integrated spectral volume depolarization ratio was implemented in an attempt to identify marine boundary layers impacted by the presence of anthropogenic aerosols and, therefore, a marine mixture designation is given when the integrated spectral volume depolarization ratio is greater than 1.5 within the aerosol layer [29].

Similarly, over IGBP land surfaces, layers are classified as polluted continental when the layer exhibits low depolarization (δ'_{1064} less than or equal to 0.15), is not elevated, the integrated spectral depolarization ratio fraction is greater than 1.5 [30], or are classified as polluted continental using MERRA-2, as discussed in further detail later in this section. Smoke layers are assigned to elevated aerosol layers with low depolarization (δ'_{1064} less than 0.15), the spectral depolarization ratio fraction is less than 1.5, or classified as smoke using MERRA-2. UTLS aerosol layers are classified as layers with low depolarization (δ'_{1064} less than 0.15), with a feature base above 10 km. The CATS operational aerosol-typing algorithm does not assign a volcanic ash type within the troposphere, as layers with high depolarization and a mid-layer temperature of $-20\,°C$ are classified as a cirrus cloud by the CAD when below the MERRA-2 tropopause height. The CATS Mode 7.2 operational aerosol-typing algorithm is very similar to the Mode 7.1 algorithm; however, the observed

inputs are limited to γ'_{1064} and δ'_{1064}. Therefore, due to the lack of spectral depolarization information, a marine mixture is not distinguished from marine and therefore is not classified, and the elevation criteria and MERRA-2 information are used to distinguish polluted continental from smoke over land (Figure 1). It should be noted that a subsequent paper will focus on lidar ratios assigned to each CATS aerosol type and CATS-derived aerosol optical properties.
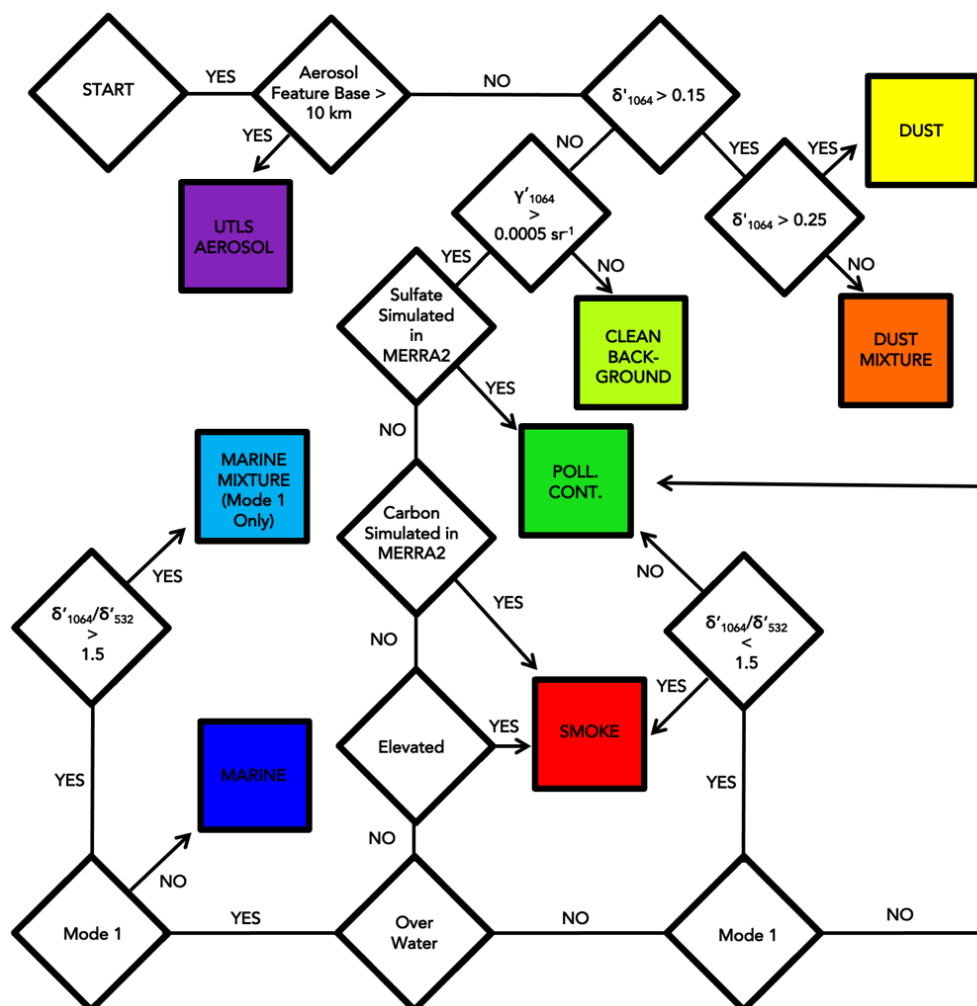
Figure 1. Schematic of the CATS aerosol-typing algorithm for both science modes.

The use of ancillary information such as the IGBP surface type and elevation criteria to distinguish the aerosol type can lead to aerosol-typing biases [28,31], which may adversely impact retrieved aerosol optical properties such as extinction. Therefore, in both Mode 7.1 and 7.2 CATS final V3-00 operational aerosol-typing algorithms, simulated aerosol information from the NASA Goddard Earth Observing System MERRA-2 reanalysis [32–34] is utilized. MERRA-2 treats aerosols with an online version of the Goddard Chemistry, Aerosol, Radiation, Transport (GOCART) model and simulates the mass of dust, seasalt, sulfate, black carbon, and organic carbon aerosols [35,36]. Notably, biomass-burning aerosol emissions in GEOS-5 are parameterized using the Quick Fire Emission Database (QFED), based on Fire Radiative Power (FRP) reported by the Moderate Resolution Imaging Spectroradiometer (MODIS) Aqua and Terra sensors [37]. Aerosol optical properties from the Optical Properties of Aerosols and Clouds (OPAC) database [38] are used for seasalt, sulfate, and carbonaceous species, while an observationally derived set of aerosol optical properties are used for dust [28,39]. In addition to meteorological observations to constrain the dynamical state of the system, MERRA-2's aerosol optical thickness

(AOT) is assimilated to constrain simulated aerosol loadings using observations from both Moderate Resolution Imaging Spectroradiometer (MODIS) Aqua and Terra sensors [40,41], the Advanced Very High Resolution Radiometer (AVHRR) [42], the Multiangle Imaging SpectroRadiometer (MISR) [43], and the Aerosol Robotic Network (AERONET) ground network of sunphotometers [44].

Following a modified methodology described in Nowottnick et al. (2015) [28], MERRA-2 aerosols are mapped to CATS aerosol types to distinguish smoke (carbonaceous dominated) from polluted continental (sulfate dominated–sulfate mixed with carbonaceous aerosols). The use of the MERRA-2-based aerosol typing is conservatively invoked only when MERRA-2 simulates a smoke or polluted continental layer at the exact altitude range observed by CATS with a minimum AOT at 532 nm of 0.05, consistent with the CATS daytime minimal detection limits for an aerosol layer at 532 nm in Mode 7.1. Following Nowottnick et al. (2015) [28], MERRA-2 aerosols are mapped to the CATS smoke aerosol type when the fraction of the total carbonaceous to the total aerosol extinction within the layer is at least 0.75. MERRA-2 aerosols are mapped to the CATS polluted continental type when the fractions of the total sulfate to the total extinction exceeds 0.75 or when the fraction of the total sulfate and carbonaceous extinctions to the total aerosol extinction is at least 0.25 individually and their combined extinction to the total aerosol extinction is at least 0.75. If aerosols simulated in MERRA-2 fail to meet these criteria, a default IGBP surface type and elevation criteria are used to distinguish smoke from polluted continental. An example of how CATS observables and MERRA-2 aerosols are used to classify the aerosol type on 6 August 2016 is provided in Figure 2. On this day, CATS flew over Africa and classified depolarizing aerosols as dust north of 10° N and non-depolarizing aerosols as smoke followed by polluted continental to the south, comparing favorably to the aerosol types observed by Suomi/NPP Deep Blue [45] (Figure S1). The MERRA-2 aerosol information was invoked to inform the transition in the aerosol type from smoke to polluted continental around 14° S.

An example showing the use of the spectral particulate depolarization ratio to discern between polluted and clean marine layers on 8 March 2015 is shown in Figure 3. Here, CATS observes a layer of relatively clean marine aerosols to the south and west of the Philippines with an average spectral particulate depolarization ratio of 1.36 (left side of Figure 3) and more polluted layers to the north and east with average spectral particulate depolarization ratios of 1.65 (right side of Figure 3). Analyzing the back trajectories, the northeastern polluted region originated near southeast China and the cleaner southwestern region over the remote Pacific Ocean (Figures S2 and S3).

In Figure 4, we present the seasonal variation in the CATS most frequently classified aerosol type below 4 km for day and night granules for 2015–2017. A key feature to note is the increased transport of Saharan dust into the Caribbean during JJA [46–48], observed by CATS. Additionally, we find the increased detection and transport of smoke associated with seasonal biomass burning over northwestern North America [49,50], the Amazon [51,52], and over central and southern Africa [53,54] in JJA and SON.

The most recent CALIOP Version 4 (V4) aerosol-typing algorithm distinguishes seven tropospheric aerosol subtypes: marine, dusty marine (new in V4), dust, polluted dust, clean continental, polluted continental/smoke, and elevated smoke. Due to the challenges in differentiating polluted continental and smoke aerosol types in the CALIOP data, the V4 algorithm combines these types together, unless the aerosol layer is elevated and is assigned as an elevated smoke layer. Additional details on the CALIOP aerosol-typing algorithm can be found in Kim et al. (2018) [31] and heritage from the Version-3 algorithm can be found in Omar et al. (2009) [24].
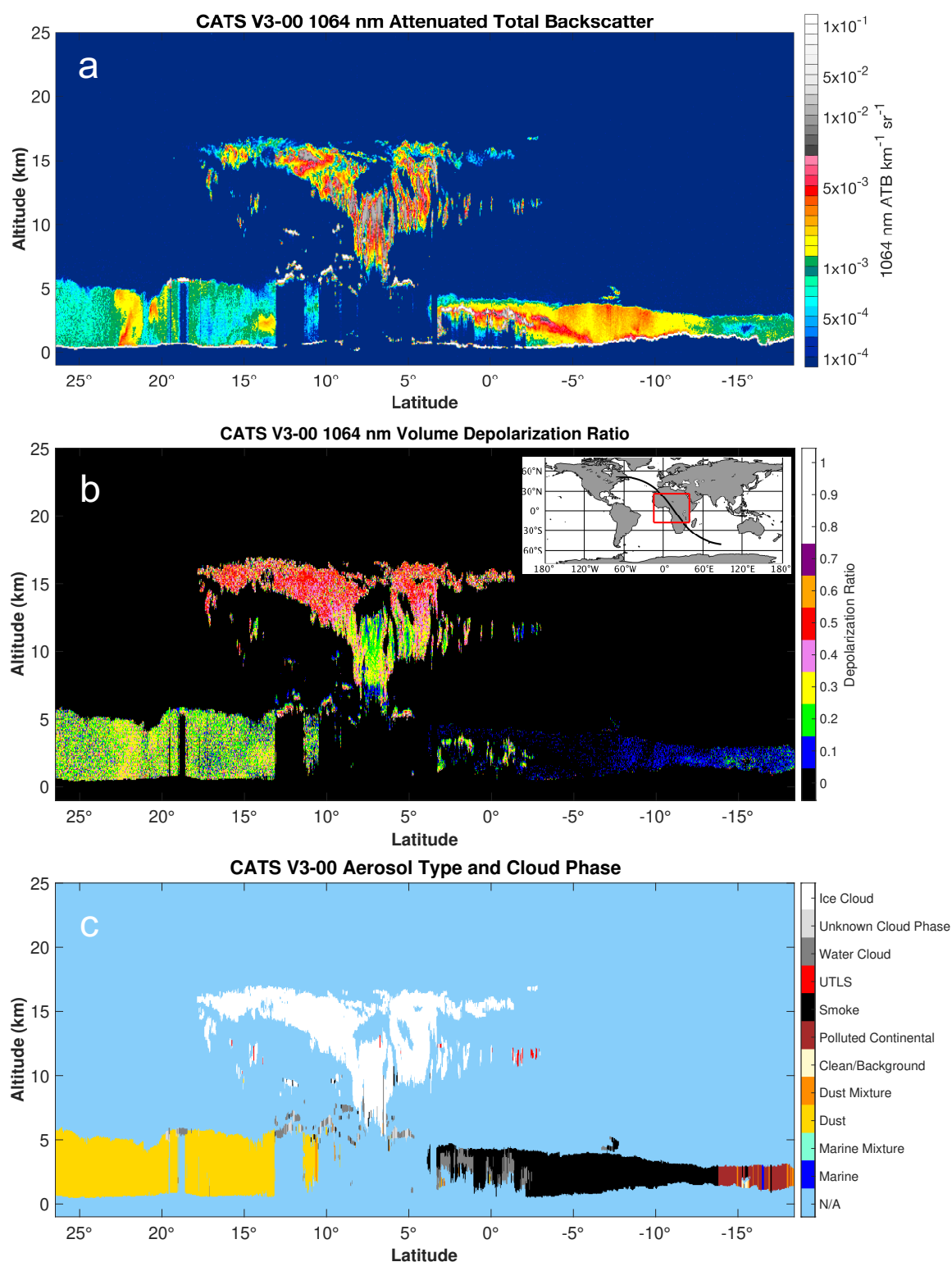
Figure 2. An example of how CATS observables and MERRA-2 aerosols were used to inform aerosol type for a subset of the CATS track (red box) on 6 August 2016. CATS 1064 nm total attenuated backscatter (**a**) and 1064 nm depolarization ratio (**b**) are used to identify features and first classify as cloud or aerosol (**c**) along with ancillary information, as described in Yorks et al., 2021 [23]. CATS observables (e.g., depolarization ratio to identify desert dust) are further used with additional ancillary information and MERRA-2 aerosols to identify aerosol type (**c**).
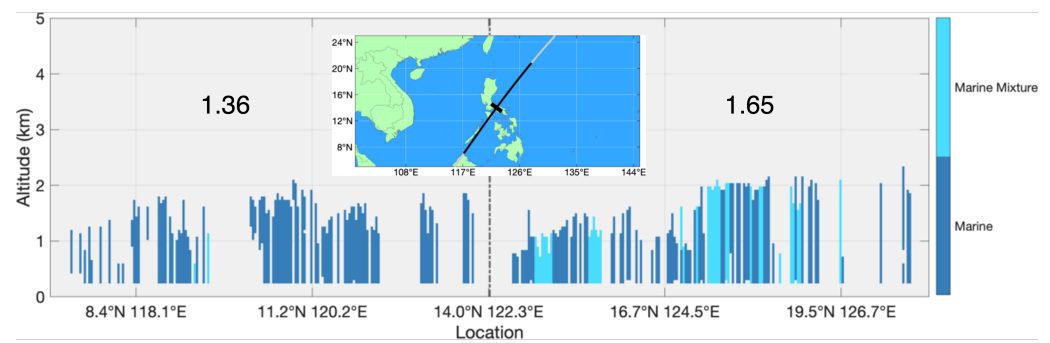
Figure 3. Effect of spectral depolarization ratios on the discernment between polluted marine and clean marine aerosol layers observed by CATS on 8 March 2015.
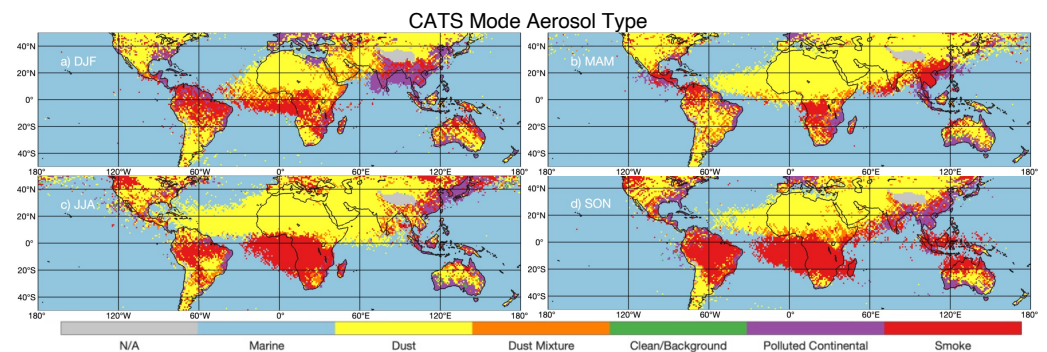
Figure 4. Seasonality of the CATS V3-00 most frequently classified aerosol type below 4 km for 2015–2017.

In Figure 5, we show the day and night 2015–2017 July, August, and September most frequently classified aerosol type between 0 and 4 km for the CATS V3-00, MERRA-2 simulated aerosols mapped to the CATS aerosol types following the methodology of Nowottnick et al. (2015) [28], and CALIOP V4.20. Comparing the CATS and CALIOP aerosol type maps, we find good agreement for dust over the Sahara and Arabian Peninsula and smoke over South American and central Africa at all altitudes. Over the western U.S. and eastern Europe, however, the CATS aerosol layers are predominately dust, while CALIOP classifies those layers as polluted dust. This difference can be attributed to differences in the thresholds and wavelengths used in each algorithm to discriminate dust from dust mixed with other aerosol types. Additionally, owing to the incorporation of the MERRA-2 aerosol information content, the V3-00 CATS algorithm depicts the downwind transport of pollution originating from Asia over the north Pacific Ocean [55,56] and smoke associated with biomass burning in the US Pacific Northwest between the surface and 4 km [49,50].
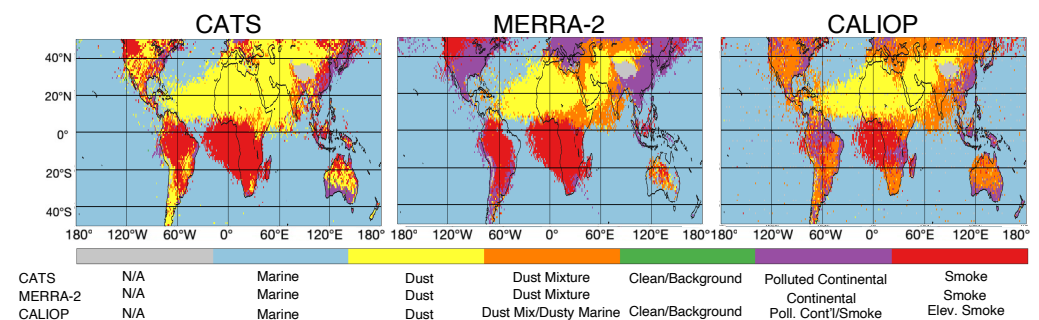
Figure 5. Comparison of the most frequently classified aerosol type below 4 km for CATS, MERRA-2, and CALIOP for JAS 2015–2017.

3. ISS Orbit Implications for Sampling of Diurnal Variability of Aerosol Vertical Distributions

Investigating the diurnal variation in clouds and aerosols from space necessitates measurements and observations throughout the daily cycle. Smoke aerosols from biomass burning have been noted to exhibit a diurnal cycle in the Maritime Continent of Southeast Asia, e.g., [17,57]. In this region, convection can be a major driver of the observed vertical aerosol altitude diurnal cycle. MPLNET is a global network of ground-based lidars and has operated since 2000 [22] providing key vertical measurements of the aerosol and cloud diurnal cycle. Many of these MPLNET sites, including the site in Kuching, Malaysia, featured in our analysis (Figure 6), are co-located with AERONET and other meteorological data collection sites. For comparison to the aerosol diurnal cycle observed by CATS, we use the quality screened MPLNET Version 3 L1.5 aerosol product, a near real-time product [58–60]. At the time of writing, fully reanalyzed MPLNET Version 3 L2 products are still being reprocessed and Kuching data were not available in the older MPLNET Version 2 archive. The differences between the Version 3 L1.5 and L2 products are generally small as both are quality assured, meaning the L1.5 is sufficient for this comparison to CATS.
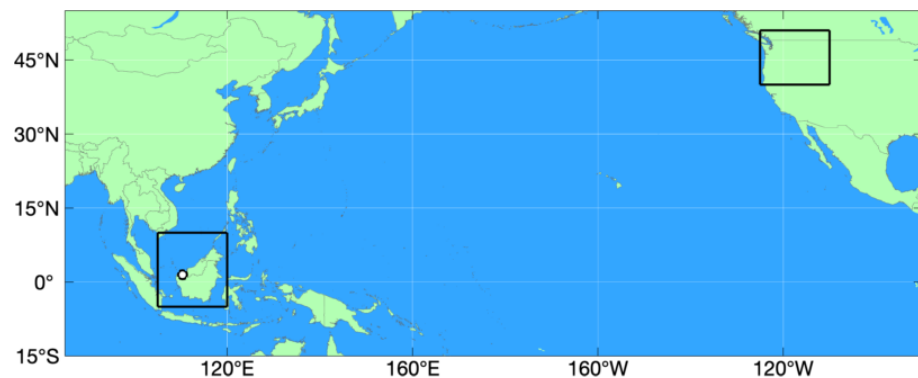
Figure 6. Map of the domains featured including the $15° \times 15°$ Southeast Asian CATS domain. The MPLNET site at Kuching, Malaysia, is denoted by a point.

Due to the differences between the daytime and nighttime sensitivities with lidars such as CATS, aerosol layers are more frequently detected at night than during the day because the minimum detectable backscatter is lower at night. This allows for more tenuous layers to be detected at night. However, there is not a discernable relationship between altitude and the layer optical depth in the CATS-detected aerosol layers in the Maritime Continent, indicating it is expected that there would be little to no diurnal bias in the extinction-weighted altitudes.

To quantify the diurnal cycle of aerosols for the regions we analyzed, we employed quality checks on the CATS L2 profile data. Aerosol typing in CATS provides a feature type score associated with the confidence in the feature being aerosol or cloud [23], similar to CALIOP [61]. As the region is plagued by clouds, we excluded UTLS (upper tropospheric/lower stratospheric) aerosols and aerosols in the profile with feature scores of less than 50% confidence to concentrate the analysis on higher-confidence aerosols rather than mistyped clouds.

For determining the diurnal cycle of aerosol altitudes, we calculated extinction-weighted altitudes (z_α) [62–64] for profiles containing any quality-checked aerosols (Equation (1)):

$$z_\alpha = \frac{\sum_{i=1}^{n} \beta_{ext,i} z_i}{\sum_{i=1}^{n} \beta_{ext,i}} \qquad (1)$$

Here, $\beta_{ext,i}$ represents the aerosol extinction of a bin, z_i the lidar bin altitude, and n the number of vertical bins within the profile. To filter outliers, bin extinction coefficients less than 0 or greater than 5 km^{-1} were omitted from the calculations. The extinction-weighted altitude provides an indication of where the peak aerosol loading is located in the profile

and provides a useful metric to compare aerosol altitudes between various instruments and models [62–64]. Processes that influence the vertical distribution of aerosols will in turn impact the evolution of the extinction-weighted altitude, such as the diurnal evolution of the planetary boundary layer (PBL), and interact with convective processes. It is worth noting that this calculation yields a single extinction-weighted altitude, which can introduce bias for complex, multi-layer aerosol scenes that are not contiguous in altitude. This metric is meant to provide a general characterization of the diurnal cycle of aerosol vertical profiles.

To calculate the change in the diurnal cycle over the island of Borneo ($15° \times 15°$ box from $105°$ E west to $120°$ E and from $5°$ S to $10°$ N) (Figure 7), these extinction-weighted altitudes were binned by UTC hour, centered over the hour (e.g., from 00:30 to 01:30 for 01:00). The altitudes represented in Figure 7 include those within the two adjacent hour bins (i.e., values for 03:00 include matching observations centered over 02:00 and 04:00). The extinction-weighted altitudes were calculated as in Equation (1) for the two years of MPLNET V3 data availability (August through October 2018 and July through November 2019).
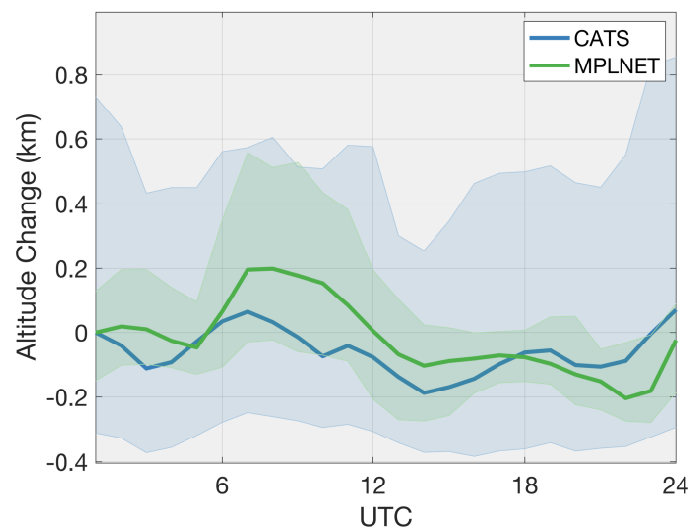
Figure 7. Observed diurnal cycle (difference from 0:00 UTC, local time UTC+8) in extinction-weighted altitudes for CATS and MPLNET for July, August, September, October, and November. Shaded region denotes the interquartile range (25–75% of data).

The median diurnal cycle of the aerosol extinction-weighted altitude in this region is statistically resolved using CATS data, with the quality assurances previously described, and compares well with the median diurnal cycle observed by the MPLNET ground-based lidar station in Kuching, Malaysia ($1.49°$ N, $110.35°$E), and generally resides within the MPLNET interquartile region (Figure 7). Specifically, the aerosol extinction-weighted altitudes increased around 200 m from the morning (0:00 UTC, local time UTC+8) in the MPLNET record and slightly less than that as observed by CATS. These altitudes peak locally in the afternoon around 7:00 UTC (15:00 local time) before decreasing in altitude into the evening hours and are consistent with the building of the mixed layer in the daily PBL cycle. In a comparison to available extinction-weighted altitudes determined from the oxygen absorption bands obtained during daylight conditions from the sun-synchronous Earth Polychromatic Imaging Camera (EPIC) [63,64], aerosol altitudes in this region also increase in the afternoon hours (Figure A1) (Methodology included in Appendix A).

In this region, the MPLNET aerosol altitudes were generally higher than those observed by CATS—on the order of 400 m (Figure S4); however, as previously discussed, data from both lidars show a similar diurnal cycle. The diurnal cycle observed by EPIC was more pronounced with altitudes increasing around 1 km from the daily altitude minimum around solar noon to sunset (Figure A1). The discrepancies between the MPLNET and CATS aerosol altitudes may be due to differences in geographical sampling or in the years

sampled (2018 and 2019 for MPLNET and 2015–2017 for CATS), as the Kuching MPLNET site was not operational during the CATS lifetime. Specifically, a large portion of the 15° × 15° CATS domain (Figure 6) was marine which is more atmospherically stable and would not exhibit as pronounced of a convective cycle as the ground site at Kuching on Borneo. Finally, discrepancies may arise due to the different measurement directions of CATS and MPLNET, as the ground-based MPLNET lidar permits measurements of aerosols below thick water clouds that would attenuate the CATS signal from space. Conversely, CATS will measure aerosols above thick water clouds where the MPLNET signal would be adversely impacted by signal attenuation.

Because the CALIOP instrument provides measurements at daily equatorial crossings corresponding to roughly 1:30 a.m./p.m., it can only provide a sample of the diurnal cycle in clouds and aerosols. For many marine domains, this sampling around the night and early afternoon may correspond to the daily minimum and maximum in vertical cloud frequency; however, for terrestrial locations, this relation may not hold [12]. Indeed, when aggregating across the breadth of the CATS record with the variety of local solar times sampled, we find many regions where the CALIOP sampling hours do not correspond to the daily minimum and maximum in the CATS vertical aerosol detection frequency (Figure 8). Two of these regions, Southeast Asia shown in Figure 6 and Northwestern North America (125° W–100° W; 40° N–51° N), feature peak July, August, and September aerosol detections in the afternoon and evening hours. These afternoon hours coincide with peak fire activity in Southeast Asia [65] and Western North America, e.g., [66,67]. In these regions, the CALIOP sampling frequency would miss the peak aerosol loading hours, highlighting the value of Earth-observing instruments in inclined orbits.
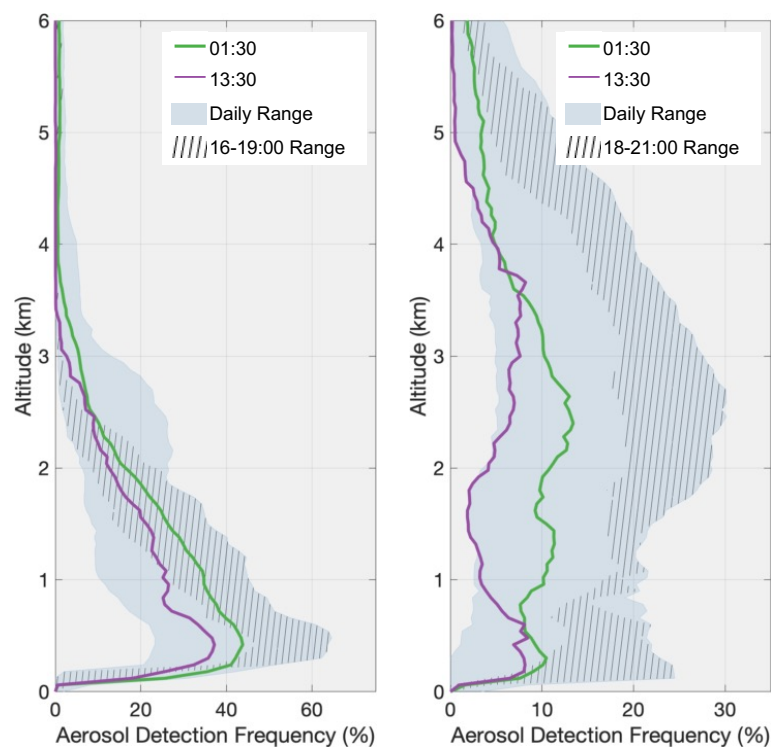
Figure 8. In 2015–2017, July, August, September, vertical aerosol detection frequencies (Aerosol CAD Score >|=5|) for the Southeast Asia region represented in Figure 6 (**left**) and for Northwestern North America (125° W–100° W; 40° N–51° N) (**right**). Blue shaded region denotes the daily range of hourly observations, black hatching for the range of observations in the peak aerosol local hours (16:00–19:00 Southeast Asia and 18:00–21:00 for Northwestern North America). Solid lines denote the hours corresponding to the A-Train crossing (green morning, purple afternoon).

4. Summary and Conclusions

During its 33 months of operation on the ISS, CATS both extended and enhanced the global climate record of aerosol vertical profiles by providing aerosol heights and types with comprehensive coverage of the tropics and mid-latitudes at local times not observed by sun-synchronous NASA sensors. Aerosol-typing algorithms use depolarization to identify dust aerosols and invoke model data to help differentiate smoke and polluted continental aerosols to mitigate the impacts of set thresholds (e.g., surface type) on aerosol typing. The CATS aerosol-typing processing algorithms leveraged the heritage of the CALIPSO algorithms, and despite relying primarily on 1064 nm observations in Mode 7.2, regional and seasonal maps of CATS aerosol types show areas dominated by marine aerosols, dust, and smoke that are very consistent with well-known aerosol source regions, CALIPSO aerosol types, and MERRA-2 data. Additionally, the $51°$ inclination angle of the ISS orbit enables estimates of the diurnal and vertical variability of aerosols in regions such as Southeast Asia, where smoke from biomass burning tracks the daily convective cycle. This paper has demonstrated that the CATS aerosol algorithms and data products have a wide range of applications such as aerosol typing and transport, aerosol particle sphericity, and diurnal variability.

CATS data users should consider limitations when analyzing CATS aerosol data, such as the mistyping of smoke and polluted continental aerosols off the west coast of South America or dust aerosols that may actually be non-spherical smoke in Southern Africa due to the burning of dry savannah in intense high-temperature fires. Furthermore, day–night SNR contrasts may hinder the ability to determine the diurnal variability of aerosols in regions with weaker aerosol loading. Future algorithms for spaceborne backscatter lidars have the potential to evolve beyond using hard threshold values for determining aerosol types, as used in the operational CALIPSO and CATS aerosol-typing algorithms, by using machine learning [23] and other techniques that utilize spatial correlations instead of determining aerosol type for a single profile independently. Finally, the next generation of space-based backscatter lidars should include multiple wavelengths of the depolarization ratio and a better SNR, specifically more similar day-to-night SNRs if in an inclined orbit, to further improve our understanding of the diurnal, seasonal, and regional variability of aerosol type, height, and extinction.

Conflicts of Interest: The authors declare no conflict of interest.

Appendix A. EPIC Aerosol Analysis

The aerosol optical centroid height (AOCH) retrieved from the EPIC (Earth Polychromatic Imaging Camera) observation adopted the oxygen absorption spectroscopy method [63,64,68]. We assume the aerosol vertical extinction profile follows a quasi-Gaussian distribution characterized by the AOD, extinction peak height, and half-width parameter. The extinction peak height retrieved by our algorithm represents the altitude where the aerosol extinction has the maximum value, so it is named as the optical centroid height. The half-width parameter is assumed as 1 km. The optical properties of the aerosol follow the smoke aerosol model in Chen et al. (2021) [69]. The algorithm first retrieves the AOD using the 443 nm EPIC channel, then derives the AOCH using the ratio of O2 A and B bands to their neighboring continuum bands (688/680 and 764/780 nm). The cloud screening is conducted through the spatial homogeneity tests at 443 and 551 nm, together with the brightness tests at 443 and 680 nm over land surface and 443, 680 and 780 nm for water surface. The retrievals with a sun glint angle lower than 30° over water surface are also screened [70]. The surface reflectance over land comes from the 10-year climatology of Lambertian surface reflectance data of the MODIS MCD43 product [71]. For over water surface, the GOME-2 Lambert-equivalent reflectivity product [72] is applied. The Unified and Linearized Vector Radiative Transfer Model (UNL-VRTM) [73] is used to generate the lookup table for the retrieval. We retrieved the EPIC AOCH over the research domain (105° E–120° E, 5° S–10° N) for July through November of 2016–2018 and calculated the hourly mean of the EPIC AOCH.
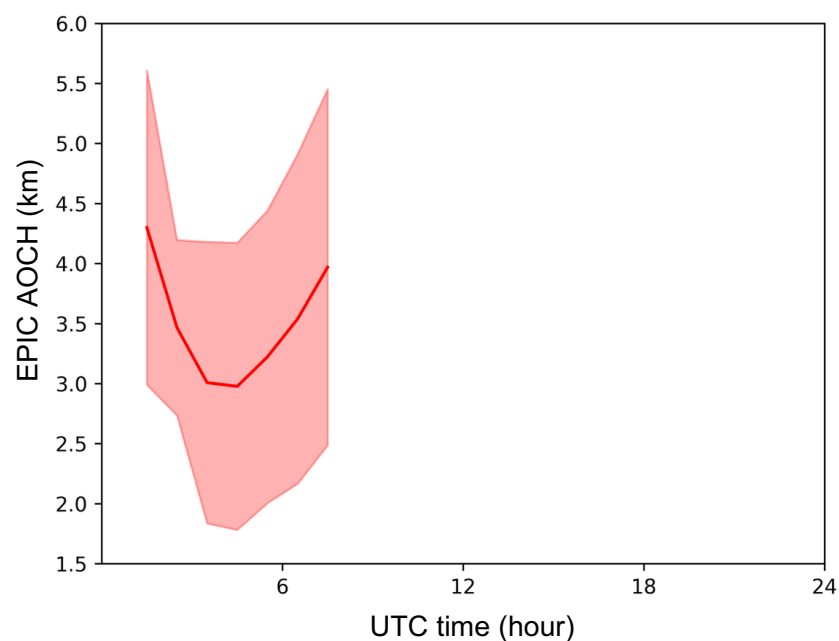
Figure A1. Diurnal cycle of July–November 2016–2018 EPIC aerosol optical centroid heights (AOCH) for the Southeast Asian region outlined in Figure 6.

References

1. Zarzycki, C.M.; Bond, T.C. How much can the vertical distribution of black carbon affect its global direct radiative forcing? *Geophys. Res. Lett.* **2010**, *37*. [CrossRef]
2. Boucher, O.; Randall, D.; Artaxo, P.; Bretherton, C.; Feingold, G.; Forster, P.; Kerminen, V.M.; Kondo, Y.; Liao, H.; Lohmann, U.; et al. Clouds and Aerosols. In *Climate Change 2013: The Physical Science Basis. Contribution of Working Group I to the Fifth Assessment Report of the Intergovernmental Panel on Climate Change*; Cambridge University Press: Cambridge, UK, 2013; pp. 571–657.
3. Crutzen, P.J.; Andreae, M.O. Biomass Burning in the Tropics: Impact on Atmospheric Chemistry and Biogeochemical Cycles. *Science* **1990**, *250*, 1669–1678. [CrossRef]
4. Ackerman, A.S.; Toon, O.B.; Stevens, D.E.; Heymsfield, A.J.; Ramanathan, V.; Welton, E.J. Reduction of Tropical Cloudiness by Soot. *Science* **2000**, *288*, 1042–1047. [CrossRef] [PubMed]
5. Samset, B.H.; Myhre, G. Vertical dependence of black carbon, sulphate and biomass burning aerosol radiative forcing. *Geophys. Res. Lett.* **2011**, *38*. [CrossRef]
6. Zhang, L.; Li, Q.B.; Gu, Y.; Liou, K.N.; Meland, B. Dust vertical profile impact on global radiative forcing estimation using a coupled chemical-transport–radiative-transfer model. *Atmos. Chem. Phys.* **2013**, *13*, 7097–7114. [CrossRef]
7. Ge, C.; Wang, J.; Reid, J.S. Mesoscale modeling of smoke transport over the Southeast Asian Maritime Continent: Coupling of smoke direct radiative effect below and above the low-level clouds. *Atmos. Chem. Phys.* **2014**, *14*, 159–174. [CrossRef]
8. Goodkind, A.L.; Tessum, C.W.; Coggins, J.S.; Hill, J.D.; Marshall, J.D. Fine-scale damage estimates of particulate matter air pollution reveal opportunities for location-specific mitigation of emissions. *Proc. Natl. Acad. Sci. USA* **2019**, *116*, 8775–8780. [CrossRef]
9. Winker, D.M.; Vaughan, M.A.; Omar, A.; Hu, Y.; Powell, K.A.; Liu, Z.; Hunt, W.H.; Young, S.A. Overview of the CALIPSO Mission and CALIOP Data Processing Algorithms. *J. Atmos. Ocean. Technol.* **2009**, *26*, 2310–2323. [CrossRef]
10. McGill, M.J.; Yorks, J.E.; Scott, V.S.; Kupchock, A.W.; Selmer, P.A. The Cloud-Aerosol Transport System (CATS): A technology demonstration on the International Space Station. In Proceedings of the Lidar Remote Sensing for Environmental Monitoring XV, San Diego, CA, USA, 9–13 August 2015; Volume 9612, p. 96120A. [CrossRef]
11. Yorks, J.E.; McGill, M.J.; Palm, S.P.; Hlavka, D.L.; Selmer, P.A.; Nowottnick, E.P.; Vaughan, M.A.; Rodier, S.D.; Hart, W.D. An overview of the CATS level 1 processing algorithms and data products. *Geophys. Res. Lett.* **2016**, *43*, 4632–4639. [CrossRef]
12. Noel, V.; Chepfer, H.; Chiriaco, M.; Yorks, J. The diurnal cycle of cloud profiles over land and ocean between 51° S and 51° N, seen by the CATS spaceborne lidar from the International Space Station. *Atmos. Chem. Phys.* **2018**, *18*, 9457–9473. [CrossRef]
13. Lee, L.; Zhang, J.; Reid, J.S.; Yorks, J.E. Investigation of CATS aerosol products and application toward global diurnal variation of aerosols. *Atmos. Chem. Phys.* **2019**, *19*, 12687–12707. [CrossRef]
14. Knippertz, P.; Todd, M.C. Mineral dust aerosols over the Sahara: Meteorological controls on emission and transport and implications for modeling. *Rev. Geophys.* **2012**, *50*. [CrossRef]
15. Hyer, E.J.; Reid, J.S.; Prins, E.M.; Hoffman, J.P.; Schmidt, C.C.; Miettinen, J.I.; Giglio, L. Patterns of fire activity over Indonesia and Malaysia from polar and geostationary satellite observations. *Atmos. Res.* **2013**, *122*, 504–519. [CrossRef]
16. Kaufman, Y.J.; Ichoku, C.; Giglio, L.; Korontzi, S.; Chu, D.A.; Hao, W.M.; Li, R.R.; Justice, C.O. Fire and smoke observed from the Earth Observing System MODIS instrument–products, validation, and operational use. *Int. J. Remote Sens.* **2003**, *24*, 1765–1781. [CrossRef]
17. Wang, J.; Christopher, S.A.; Nair, U.S.; Reid, J.S.; Prins, E.M.; Szykman, J.; Hand, J.L. Mesoscale modeling of Central American smoke transport to the United States: 1. "Top-down" assessment of emission strength and diurnal variation impacts. *J. Geophys. Res. Atmos.* **2006**, *111*. [CrossRef]
18. Heinold, B.; Knippertz, P.; Marsham, J.H.; Fiedler, S.; Dixon, N.S.; Schepanski, K.; Laurent, B.; Tegen, I. The role of deep convection and nocturnal low-level jets for dust emission in summertime West Africa: Estimates from convection-permitting simulations. *J. Geophys. Res. Atmos.* **2013**, *118*, 4385–4400. [CrossRef]
19. Zhang, J.; Zuidema, P. The diurnal cycle of the smoky marine boundary layer observed during August in the remote southeast Atlantic. *Atmos. Chem. Phys.* **2019**, *19*, 14493–14516. [CrossRef]
20. Hodzic, A.; Duvel, J.P. Impact of Biomass Burning Aerosols on the Diurnal Cycle of Convective Clouds and Precipitation Over a Tropical Island. *J. Geophys. Res. Atmos.* **2018**, *123*, 1017–1036. [CrossRef]
21. Li, Z.; Guo, J.; Ding, A.; Liao, H.; Liu, J.; Sun, Y.; Wang, T.; Xue, H.; Zhang, H.; Zhu, B. Aerosol and boundary-layer interactions and impact on air quality. *Natl. Sci. Rev.* **2017**, *4*, 810–833. [CrossRef]
22. Welton, E.J.; Campbell, J.R.; Spinhirne, J.D.; Scott, V.S. Global monitoring of clouds and aerosols using a network of micropulse lidar systems. *Lidar Remote Sens. Ind. Environ. Monit.* **2001**, *4153*, 151–158. [CrossRef]
23. Yorks, J.E.; Selmer, P.A.; Kupchock, A.; Nowottnick, E.P.; Christian, K.E.; Rusinek, D.; Dacic, N.; McGill, M.J. Aerosol and Cloud Detection Using Machine Learning Algorithms and Space-Based Lidar Data. *Atmosphere* **2021**, *12*, 606. [CrossRef]
24. Omar, A.H.; Winker, D.M.; Vaughan, M.A.; Hu, Y.; Trepte, C.R.; Ferrare, R.A.; Lee, K.P.; Hostetler, C.A.; Kittaka, C.; Rogers, R.R.; et al. The CALIPSO Automated Aerosol Classification and Lidar Ratio Selection Algorithm. *J. Atmos. Ocean. Technol.* **2009**, *26*, 1994–2014. [CrossRef]

25. Loveland, T.R.; Reed, B.C.; Brown, J.F.; Ohlen, D.O.; Zhu, Z.; Yang, L.; Merchant, J.W. Development of a global land cover characteristics database and IGBP DISCover from 1 km AVHRR data. *Int. J. Remote Sens.* **2000**, *21*, 1303–1330. [CrossRef]

26. Nowottnick, E.; Colarco, P.; da Silva, A.; Hlavka, D.; McGill, M. The fate of saharan dust across the atlantic and implications for a central american dust barrier. *Atmos. Chem. Phys.* **2011**, *11*, 8415–8431. [CrossRef]

27. Braun, S.A.; Newman, P.A.; Heymsfield, G.M. NASA's Hurricane and Severe Storm Sentinel (HS3) Investigation. *Bull. Am. Meteorol. Soc.* **2016**, *97*, 2085–2102. [CrossRef]

28. Nowottnick, E.P.; Colarco, P.R.; Welton, E.J.; da Silva, A. Use of the CALIOP vertical feature mask for evaluating global aerosol models. *Atmos. Meas. Tech.* **2015**, *8*, 3647–3669. [CrossRef]

29. Burton, S.P.; Vaughan, M.A.; Ferrare, R.A.; Hostetler, C.A. Separating mixtures of aerosol types in airborne High Spectral Resolution Lidar data. *Atmos. Meas. Tech.* **2014**, *7*, 419–436. [CrossRef]

30. Burton, S.P.; Ferrare, R.A.; Hostetler, C.A.; Hair, J.W.; Rogers, R.R.; Obland, M.D.; Butler, C.F.; Cook, A.L.; Harper, D.B.; Froyd, K.D. Aerosol classification using airborne High Spectral Resolution Lidar measurements—Methodology and examples. *Atmos. Meas. Tech.* **2012**, *5*, 73–98. [CrossRef]

31. Kim, M.H.; Omar, A.H.; Tackett, J.L.; Vaughan, M.A.; Winker, D.M.; Trepte, C.R.; Hu, Y.; Liu, Z.; Poole, L.R.; Pitts, M.C.; et al. The CALIPSO version 4 automated aerosol classification and lidar ratio selection algorithm. *Atmos. Meas. Tech.* **2018**, *11*, 6107–6135. [CrossRef]

32. Gelaro, R.; McCarty, W.; Suárez, M.J.; Todling, R.; Molod, A.; Takacs, L.; Randles, C.A.; Darmenov, A.; Bosilovich, M.G.; Reichle, R.; et al. The Modern-Era Retrospective Analysis for Research and Applications, Version 2 (MERRA-2). *J. Clim.* **2017**, *30*, 5419–5454. [CrossRef]

33. Randles, C.A.; Silva, A.M.d.; Buchard, V.; Colarco, P.R.; Darmenov, A.; Govindaraju, R.; Smirnov, A.; Holben, B.; Ferrare, R.; Hair, J.; et al. The MERRA-2 Aerosol Reanalysis, 1980 Onward. Part I: System Description and Data Assimilation Evaluation. *J. Clim.* **2017**, *30*, 6823–6850. [CrossRef] [PubMed]

34. Buchard, V.; Randles, C.A.; Silva, A.M.d.; Darmenov, A.; Colarco, P.R.; Govindaraju, R.; Ferrare, R.; Hair, J.; Beyersdorf, A.J.; Ziemba, L.D.; et al. The MERRA-2 Aerosol Reanalysis, 1980 Onward. Part II: Evaluation and Case Studies. *J. Clim.* **2017**, *30*, 6851–6872. [CrossRef] [PubMed]

35. Chin, M.; Ginoux, P.; Kinne, S.; Torres, O.; Holben, B.N.; Duncan, B.N.; Martin, R.V.; Logan, J.A.; Higurashi, A.; Nakajima, T. Tropospheric Aerosol Optical Thickness from the GOCART Model and Comparisons with Satellite and Sun Photometer Measurements. *J. Atmos. Sci.* **2002**, *59*, 461–483. [CrossRef]

36. Colarco, P.; Silva, A.d.; Chin, M.; Diehl, T. Online simulations of global aerosol distributions in the NASA GEOS-4 model and comparisons to satellite and ground-based aerosol optical depth. *J. Geophys. Res. Atmos.* **2010**, *115*. [CrossRef]

37. Darmenov, A.S.; da Silva, A. The Quick Fire Emissions Dataset (QFED): Documentation of versions 2.1, 2.2 and 2.4. In *Technical Report Series on Global Modeling and Data Assimilation*; National Aeronautics and Space Administration: Washington, DC, USA, 2015; Volume 38, p. 212.

38. Hess, M.; Koepke, P.; Schult, I. Optical Properties of Aerosols and Clouds: The Software Package OPAC. *Bull. Am. Meteorol. Soc.* **1998**, *79*, 831–844. [CrossRef]

39. Colarco, P.R.; Nowottnick, E.P.; Randles, C.A.; Yi, B.; Yang, P.; Kim, K.M.; Smith, J.A.; Bardeen, C.G. Impact of radiatively interactive dust aerosols in the NASA GEOS-5 climate model: Sensitivity to dust particle shape and refractive index. *J. Geophys. Res. Atmos.* **2014**, *119*, 753–786. [CrossRef]

40. Remer, L.A.; Kaufman, Y.J.; Tanré, D.; Mattoo, S.; Chu, D.A.; Martins, J.V.; Li, R.R.; Ichoku, C.; Levy, R.C.; Kleidman, R.G.; et al. The MODIS Aerosol Algorithm, Products, and Validation. *J. Atmos. Sci.* **2005**, *62*, 947–973. [CrossRef]

41. Levy, R.C.; Remer, L.A.; Kleidman, R.G.; Mattoo, S.; Ichoku, C.; Kahn, R.; Eck, T.F. Global evaluation of the Collection 5 MODIS dark-target aerosol products over land. *Atmos. Chem. Phys.* **2010**, *10*, 10399–10420. [CrossRef]

42. Heidinger, A.K.; Foster, M.J.; Walther, A.; Zhao, X.T. The Pathfinder Atmospheres–Extended AVHRR Climate Dataset. *Bull. Am. Meteorol. Soc.* **2014**, *95*, 909–922. [CrossRef]

43. Kahn, R.A.; Gaitley, B.J.; Martonchik, J.V.; Diner, D.J.; Crean, K.A.; Holben, B. Multiangle Imaging Spectroradiometer (MISR) global aerosol optical depth validation based on 2 years of coincident Aerosol Robotic Network (AERONET) observations. *J. Geophys. Res. Atmos.* **2005**, *110*. [CrossRef]

44. Holben, B.N.; Eck, T.F.; Slutsker, I.; Tanré, D.; Buis, J.P.; Setzer, A.; Vermote, E.; Reagan, J.A.; Kaufman, Y.J.; Nakajima, T.; et al. AERONET—A Federated Instrument Network and Data Archive for Aerosol Characterization. *Remote Sens. Environ.* **1998**, *66*, 1–16. [CrossRef]

45. Hsu, N.C.; Lee, J.; Sayer, A.M.; Kim, W.; Bettenhausen, C.; Tsay, S.C. VIIRS Deep Blue Aerosol Products Over Land: Extending the EOS Long-Term Aerosol Data Records. *J. Geophys. Res. Atmos.* **2019**, *124*, 4026–4053. [CrossRef]

46. Chiapello, I.; Moulin, C. TOMS and METEOSAT satellite records of the variability of Saharan dust transport over the Atlantic during the last two decades (1979–1997). *Geophys. Res. Lett.* **2002**, *29*, 17-1–17-4. [CrossRef]

47. Karyampudi, V.M.; Palm, S.P.; Reagen, J.A.; Fang, H.; Grant, W.B.; Hoff, R.M.; Moulin, C.; Pierce, H.F.; Torres, O.; Browell, E.V.; et al. Validation of the Saharan Dust Plume Conceptual Model Using Lidar, Meteosat, and ECMWF Data. *Bull. Am. Meteorol. Soc.* **1999**, *80*, 1045–1076. [CrossRef]

48. Carlson, T.N.; Prospero, J.M. The Large-Scale Movement of Saharan Air Outbreaks over the Northern Equatorial Atlantic. *J. Appl. Meteorol. Climatol.* **1972**, *11*, 283–297. [CrossRef]

49. Christian, K.; Wang, J.; Ge, C.; Peterson, D.; Hyer, E.; Yorks, J.; McGill, M. Radiative Forcing and Stratospheric Warming of Pyrocumulonimbus Smoke Aerosols: First Modeling Results With Multisensor (EPIC, CALIPSO, and CATS) Views from Space. *Geophys. Res. Lett.* **2019**, *46*, 10061–10071. [CrossRef]

50. Peterson, D.A.; Hyer, E.J.; Campbell, J.R.; Fromm, M.D.; Hair, J.W.; Butler, C.F.; Fenn, M.A. The 2013 Rim Fire: Implications for Predicting Extreme Fire Spread, Pyroconvection, and Smoke Emissions. *Bull. Am. Meteorol. Soc.* **2015**, *96*, 229–247. [CrossRef]

51. Gonzalez-Alonso, L.; Val Martin, M.; Kahn, R.A. Biomass-burning smoke heights over the Amazon observed from space. *Atmos. Chem. Phys.* **2019**, *19*, 1685–1702. [CrossRef]

52. Holben, B.N.; Setzer, A.; Eck, T.F.; Pereira, A.; Slutsker, I. Effect of dry-season biomass burning on Amazon basin aerosol concentrations and optical properties, 1992–1994. *J. Geophys. Res. Atmos.* **1996**, *101*, 19465–19481. [CrossRef]

53. Eck, T.F.; Holben, B.N.; Reid, J.S.; Mukelabai, M.M.; Piketh, S.J.; Torres, O.; Jethva, H.T.; Hyer, E.J.; Ward, D.E.; Dubovik, O.; et al. A seasonal trend of single scattering albedo in southern African biomass-burning particles: Implications for satellite products and estimates of emissions for the world's largest biomass-burning source. *J. Geophys. Res. Atmos.* **2013**, *118*, 6414–6432. [CrossRef]

54. Herman, J.R.; Bhartia, P.K.; Torres, O.; Hsu, C.; Seftor, C.; Celarier, E. Global distribution of UV-absorbing aerosols from Nimbus 7/TOMS data. *J. Geophys. Res. Atmos.* **1997**, *102*, 16911–16922. [CrossRef]

55. Di Pierro, M.; Jaeglé, L.; Anderson, T.L. Satellite observations of aerosol transport from East Asia to the Arctic: Three case studies. *Atmos. Chem. Phys.* **2011**, *11*, 2225–2243. [CrossRef]

56. Yu, H.; Remer, L.A.; Chin, M.; Bian, H.; Kleidman, R.G.; Diehl, T. A satellite-based assessment of transpacific transport of pollution aerosol. *J. Geophys. Res. Atmos.* **2008**, *113*. [CrossRef]

57. Campbell, J.R.; Ge, C.; Wang, J.; Welton, E.J.; Bucholtz, A.; Hyer, E.J.; Reid, E.A.; Chew, B.N.; Liew, S.C.; Salinas, S.V.; et al. Applying Advanced Ground-Based Remote Sensing in the Southeast Asian Maritime Continent to Characterize Regional Proficiencies in Smoke Transport Modeling. *J. Appl. Meteorol. Climatol.* **2016**, *55*, 3–22. [CrossRef]

58. Welton, E.J.; Stewart, S.A.; Lewis, J.R.; Belcher, L.R.; Campbell, J.R.; Lolli, S. Status of the NASA Micro Pulse Lidar Network (MPLNET): Overview of the network and future plans, new version 3 data products, and the polarized MPL. *EPJ Web Conf.* **2018**, *176*, 09003. [CrossRef]

59. Welton, E.J.; Voss, K.J.; Gordon, H.R.; Maring, H.; Smirnov, A.; Holben, B.; Schmid, B.; Livingston, J.M.; Durkee, P.A.; Formenti, P.; et al. Ground-based lidar measurements of aerosols during ACE-2: Instrument description, results, and comparisons with other ground-based and airborne measurements. *Tellus Chem. Phys. Meteorol.* **2000**, *52*, 636–651. [CrossRef]

60. Welton, E.J.; Voss, K.J.; Quinn, P.K.; Flatau, P.J.; Markowicz, K.; Campbell, J.R.; Spinhirne, J.D.; Gordon, H.R.; Johnson, J.E. Measurements of aerosol vertical profiles and optical properties during INDOEX 1999 using micropulse lidars. *J. Geophys. Res. Atmos.* **2002**, *107*, INX2 18-1–INX2 18-20. [CrossRef]

61. Liu, Z.; Kar, J.; Zeng, S.; Tackett, J.; Vaughan, M.; Avery, M.; Pelon, J.; Getzewich, B.; Lee, K.P.; Magill, B.; et al. Discriminating between clouds and aerosols in the CALIOP version 4.1 data products. *Atmos. Meas. Tech.* **2019**, *12*, 703–734. [CrossRef]

62. Koffi, B.; Schulz, M.; Bréon, F.M.; Griesfeller, J.; Winker, D.; Balkanski, Y.; Bauer, S.; Berntsen, T.; Chin, M.; Collins, W.D.; et al. Application of the CALIOP layer product to evaluate the vertical distribution of aerosols estimated by global models: AeroCom phase I results. *J. Geophys. Res. Atmos.* **2012**, *117*. [CrossRef]

63. Xu, X.; Wang, J.; Wang, Y.; Zeng, J.; Torres, O.; Yang, Y.; Marshak, A.; Reid, J.; Miller, S. Passive remote sensing of altitude and optical depth of dust plumes using the oxygen A and B bands: First results from EPIC/DSCOVR at Lagrange-1 point. *Geophys. Res. Lett.* **2017**, *44*, 7544–7554. [CrossRef]

64. Xu, X.; Wang, J.; Wang, Y.; Zeng, J.; Torres, O.; Reid, J.S.; Miller, S.D.; Martins, J.V.; Remer, L.A. Detecting layer height of smoke aerosols over vegetated land and water surfaces via oxygen absorption bands: Hourly results from EPIC/DSCOVR in deep space. *Atmos. Meas. Tech.* **2019**, *12*, 3269–3288. [CrossRef]

65. Giglio, L. Characterization of the tropical diurnal fire cycle using VIRS and MODIS observations. *Remote Sens. Environ.* **2007**, *108*, 407–421. [CrossRef]

66. Beall, H. Diurnal and seasonal fluctuation of fire-hazard in pine forests. *For. Chron.* **1934**, *10*, 209–225. [CrossRef]

67. Jaffe, D.A.; O'Neill, S.M.; Larkin, N.K.; Holder, A.L.; Peterson, D.L.; Halofsky, J.E.; Rappold, A.G. Wildfire and prescribed burning impacts on air quality in the United States. *J. Air Waste Manag. Assoc.* **2020**, *70*, 583–615. [CrossRef]

68. Lu, Z.; Wang, J.; Xu, X.; Chen, X.; Kondragunta, S.; Torres, O.; Wilcox, E.M.; Zeng, J. Hourly Mapping of the Layer Height of Thick Smoke Plumes over the Western U.S. in 2020 Severe Fire Season. *Front. Remote Sens.* **2021**, *2*, 766628. [CrossRef]

69. Chen, X.; Wang, J.; Xu, X.; Zhou, M.; Zhang, H.; Castro Garcia, L.; Colarco, P.R.; Janz, S.J.; Yorks, J.; McGill, M.; et al. First retrieval of absorbing aerosol height over dark target using TROPOMI oxygen B band: Algorithm development and application for surface particulate matter estimates. *Remote Sens. Environ.* **2021**, *265*, 112674. [CrossRef]

70. Levy, R.C.; Mattoo, S.; Munchak, L.A.; Remer, L.A.; Sayer, A.M.; Patadia, F.; Hsu, N.C. The Collection 6 MODIS aerosol products over land and ocean. *Atmos. Meas. Tech.* **2013**, *6*, 2989–3034. [CrossRef]

71. Schaaf, C.B.; Gao, F.; Strahler, A.H.; Lucht, W.; Li, X.; Tsang, T.; Strugnell, N.C.; Zhang, X.; Jin, Y.; Muller, J.P.; et al. First operational BRDF, albedo nadir reflectance products from MODIS. *Remote Sens. Environ.* **2002**, *83*, 135–148. [CrossRef]

72. Tilstra, L.G.; Tuinder, O.N.E.; Wang, P.; Stammes, P. Surface reflectivity climatologies from UV to NIR determined from Earth observations by GOME-2 and SCIAMACHY. *J. Geophys. Res. Atmos.* **2017**, *122*, 4084–4111. [CrossRef]

73. Wang, J.; Xu, X.; Ding, S.; Zeng, J.; Spurr, R.; Liu, X.; Chance, K.; Mishchenko, M. A numerical testbed for remote sensing of aerosols, and its demonstration for evaluating retrieval synergy from a geostationary satellite constellation of GEO-CAPE and GOES-R. *J. Quant. Spectrosc. Radiat. Transf.* **2014**, *146*, 510–528. [CrossRef]